# Electromechanical analysis of functionally graded panels with surface-integrated piezo-patches for optimal energy harvesting

Peyman Lahe Motlagh[a], Mirmeysam Rafiei Anamagh[b], Bekir Bediz[b,*], Ipek Basdogan[a]

[a] *Mechanical Engineering Department, Koc University, Istanbul, 34450, TURKEY*

[b] *Faculty of Engineering and Natural Sciences, Sabanci University, Istanbul, 34956, TURKEY*

**Abstract**

This paper presents an electromechanical modeling approach for predicting the dynamics of (straight/curved) functionally graded panels with multiple surface-integrated piezo-patches. Bi-axial material variation is considered using the theory of mixture approach. The governing equations are derived following the first order shear deformation theory and the Hamilton's principle. The derived boundary value problem is solved numerically using a meshless approach based on Chebyshev polynomials. Mass and stiffness contributions of piezo-patch(es) as well as two-way electromechanical coupling behavior are incorporated both for modal and harmonic analyses. To validate the accuracy of the presented solution technique, the results for various cases are compared to those obtained from finite-element analyses. It is shown that the maximum difference in the predicted natural frequencies is below 1%, but for a fraction of the computational time. Furthermore, the harmonic analysis results excellently match FE results. Note that material variation changes the spatial stiffness of the panel and thus, the functionally graded panel can be designed according to a predefined objective function using the proposed modeling approach. As a demonstration, specific to energy harvesting application, the voltage/power output was maximized through material and geometry/shape variations. It was demonstrated that significant improvements can be achieved through the presented methodology.

*Key words:* energy harvesting, piezoelectric, functionally graded materials, doubly-curved, Chebyshev.

## 1. Introduction

Functionally graded materials (FGMs) are one of the emerging composite materials used in diverse fields of engineering such as automotive and aerospace industries [1–4]. FGMs are made from different phases of material constituents and yields a smooth/continuous transition of material properties; thereby eliminate problems such as delamination and matrix cracking problems observed in laminated composite structures [2, 5, 6]. Furthermore, in FGM structures, the material properties such as elastic modulus and density can be tailored to achieve design requirements by changing the volume fraction of the constitutes and gradation rate in one or more specific directions [7–13]. Commonly, theory of mixtures [14, 15] or Mori Tanaka [14, 16–18] approach is used to determine the local effective material properties. In the theory of mixtures, the material properties of the composite structure is found as a linear combination of the constitute materials, whereas in the Mori Tanaka approach, the material properties are found using Eshelby's elasticity solution.

*E-mail: bbediz@sabanciuniv.edu
[1]Phone: +90-216-483-9543

The use of piezoelectric materials by either embedding into or surface bonding/integration onto structures as electro-mechanical transducers (both as sensors and as actuators) enhances the structural capabilities. These smart structures have been used for a wide range of applications such as vibration or buckling control [11, 19, 20], energy harvesting [21, 22], and shunt damping [23, 24]. More recently, FGM structures used together with piezo materials have received significant attention to benefit from the unique properties of both piezo materials and FGMs.

There are many studies in the literature on the piezoelectric materials embedded on plate structures [25–31]. The majority of these studies are focused on the analysis of straight isotropic panels. In one of the earlier studies, De Marqui *et al.* [27] presented an electromechanical finite element (FE) model to predict the power output of plate-like piezoelectric energy harvesters. In their study, the governing equations are obtained following classical plate theory (CPT) and fully covered unimorph piezoelectric energy harvester configuration. Later, Aridogan *et al.* [29] predicted electromechanical response of single/multiple piezoelectric patches by neglecting their mass and inertia contributions. This assumption has been used in many similar studies such as Darabi *et al.*'s studies [32, 33] or Yoon *et al.*'s study [34]; however, note that it may lead to inaccuracy when piezo patch sizes are comparable to the host plate (*i.e.* when the electromechanical coupling between the host plate and the piezo is not weak). Therefore, there is still a need to develop a more generalized model that can predict the electromechanical coupling of curved structures integrated with patches that cover the surface of the host plate partially. For instance, Gozum *et al.* [22] modeled the electromechanical behavior of surface-bonded piezo patches on a thin plate including the mass and stiffness effects of the piezo using Heaviside functions with Rayleigh-Ritz approach. More recently, Motlagh *et.al.* [31] developed an accurate and computationally efficient modeling framework based on the first order shear deformation theory (FSDT) and spectral Chebyshev approach which can also predict the response of moderately thick and doubly-curved panels including the mass and inertia contribution of the piezo-patches.

In the case of smart FGM structures (*i.e.* FGM structures with embedded/attached piezoelectric layers/patches), the modeling approach should also be capable of capturing the varying material property of the structure along the specified directions. Although 3D modeling approaches can accurately capture the dynamics of the FGM structures, due to the high computational cost, two dimensional (2D) modeling techniques such as equivalent single layer (ESL) [35] and layer-wise (LW) [36] approaches are mostly preferred. He *et al.* [26] and Liew *et al.* [37] developed a finite element (FE) shell model based on CPT for active control of FGM structures with fully covered or partial piezoelectric layers. Similarly, Mirzaeifar *et al.* [38] used FE modeling approach based on CPT and showed that the natural frequency of the FGM structure can be optimized. Later, Shariyat presented that the dynamic buckling of FGM panels can be controlled using non-linear FE simulations based on higher shear deformation theories (HSDT) [39, 40]. To increase the computational efficiency of the FE based modeling approaches, Carrera and Valvano [41] proposed a variable kinematic model in which ESL and layer-wise approaches are used together. In their study, the modeling was performed following Carrera Unified Formulation (CUF) and it was shown that static analysis of multilayered structures can be efficiently performed compared to fully later-wise theories. Later, they proposed a new class of finite elements to predict the electromechanical dynamics of laminated shells [42]. In this modeling approach, they used a node dependent kinematics in their FE formulation so that their refined models are used only at certain regions where complex stress and/or strain distributions or strong electromechanical coupling are observed.

As aforementioned, there are various studies on FGM structures with piezoelectric layers or with surface-integrated piezo-patches; however the electromechanical modeling is performed based on FE approaches in most of these studies. In this study, to increase the computational efficiency while preserving the accuracy/precision of the results, a meshless solution approach is presented. The model is based on authors' previous studies [30, 31] where dynamic behavior of a smart (doubly-) curved isotropic host structure including piezoelectric patches is studied using FSDT kinematic equations. Here, the modeling approach is extended to predict the dynamics of a bi-directional FGM host structure with multiple surface-integrated piezo-patches. The derived governing electro-mechanical equations are solved to obtain mechanical and volt-

age frequency response functions (FRFs) using a meshless approach based on Chebyshev polynomials. The efficacy of the solution approach is demonstrated comparing the results to those found using a commercial FE software. It is also shown that the presented modeling approach can be used to tailor the material distribution along the selected directions and design the FGM panel to increase the power output in energy harvesting applications.

## 2. Problem statement

### *2.1. Functionally graded (doubly-curved) panel with multiple surface integrated piezo-patches*

Figure 1 depicts a (doubly-) curved FGM panel with bi-morph surface-integrated piezo-patches. The dimensions of the panel and piezo-patches are denoted by $a_s$, $b_s$, $h_s$ and $a_{p_k}$, $b_{p_k}$, $h_{p_k}$ along $x$, $y$, and $z$ directions, respectively; where subscripts $s$ and $p_k$ denotes the host panel and the $k^{th}$ piezo-patch. The curvature amounts of the base panel are represented by $r_1$ and $r_2$ around $x$ and $y$ directions, respectively. Note that, the piezo-patches can be connected either in parallel such that all piezo-patches are interconnected and connected to the same load, or independently where each patch is connected to a separate electrical circuit.

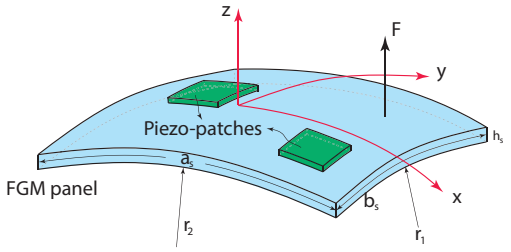


Figure 1: Schematic of a doubly-curved FGM panel with multiple surface-integrated piezo-patches.

The material variation of the FGM panel is assumed to be along the $x$ and $y$ directions. To define the volume fraction distributions of the constituent materials ($V_{\text{mat}_1}$ and $V_{\text{mat}_2}$), power-law function [43] is commonly used as follows:

$$V_{\text{mat}_1}(x,y) = \left(\frac{1}{2} + \frac{|x|}{a_s}\right)^p \left(\frac{1}{2} + \frac{|y|}{b_s}\right)^q \tag{1}$$

$$V_{\text{mat}_2}(x,y) = 1 - V_{mat_1}(x,y) \tag{2}$$

Here, $p$ and $q$ are the power-law indices that indicates the material variation rate along the $x$ and $y$ directions, respectively. Following the rule of mixture, the spatial effective material property, $\chi(x,y)$, can be predicted as:

$$\chi(x,y) = \chi_{\text{mat}_1} V_{\text{mat}_1}(x,y) + \chi_{\text{mat}_2} V_{\text{mat}_2}(x,y) \tag{3}$$

where $\chi_{\text{mat}_1}$ and $\chi_{\text{mat}_2}$ are the material properties of the constituent materials such as Young's modulus ($E$), Poisson's ratio ($\nu$) or density ($\rho$). Thus, depending on the material variation (*i.e.* gradation amount and rate) in the structure, the local compliance of the structure can be tailored.

### *2.2. Derivation of the boundary value problem*

To derive the governing boundary value problem (BVP), Hamilton's principle is used. Following the FSDT assumption [31, 44], the kinetic energy of the electro-mechanical system can be written as a summation of

kinetic energies of the host panel and the piezo-patches:

$$T = T_s + \sum_{k=1}^{n} (T_p)_k \tag{4}$$

where

$$\begin{aligned} T_s &= \frac{1}{2}\int_{V_s} \rho_s \left[ \left(\frac{\partial u_0}{\partial t}\right)_s^2 + \left(\frac{\partial v_0}{\partial t}\right)_s^2 + \left(\frac{\partial w_0}{\partial t}\right)_s^2 + z^2\left(\frac{\partial \phi_x}{\partial t}\right)_s^2 + z^2\left(\frac{\partial \phi_y}{\partial t}\right)_s^2 \right] \mathrm{d}V_s \\ &= \frac{1}{2}\int_{V_s} \rho_s \dot{\mathbf{q}}_s^{\mathrm{T}} \mathbf{\Lambda}_{q_s} \dot{\mathbf{q}}_s \mathrm{d}V_s \end{aligned} \tag{5}$$

$$\begin{aligned} (T_p)_k &= \left\{ \frac{1}{2}\int_{V_p} \rho_p \left[ \left(\frac{\partial u_0}{\partial t}\right)_p^2 + \left(\frac{\partial v_0}{\partial t}\right)_p^2 + \left(\frac{\partial w_0}{\partial t}\right)_p^2 + z^2\left(\frac{\partial \phi_x}{\partial t}\right)_p^2 + z^2\left(\frac{\partial \phi_y}{\partial t}\right)_p^2 \right] \mathrm{d}V_p \right\}_k \\ &= \left\{ \frac{1}{2}\int_{V_p} \rho_p \dot{\mathbf{q}}_p^{\mathrm{T}} \mathbf{\Lambda}_{q_p} \dot{\mathbf{q}}_p \mathrm{d}V_p \right\}_k \end{aligned} \tag{6}$$

Here, $u_0$, $v_0$, and $w_0$ are the deformations of any point on the neutral surface of the panel along $x$, $y$, and $z$ directions; $\phi_x$ and $\phi_y$ are the rotations around $y$ and $x$-axes, respectively; and form the deflection vector $\mathbf{q} = \{\mathbf{u}_0; \mathbf{v}_0; \mathbf{w}_0; \boldsymbol{\phi}_x; \boldsymbol{\phi}_y\}$; $z$ defines the distance of any point with respect to the neutral surface of the panel; $\rho$ is the density, $V$ is the volume; $n$ is the number of piezoelectric patches.

Similarly, the potential energy can be written as,

$$U = U_s + \sum_{k=1}^{n} (U_p)_k \tag{7}$$

where

$$U_s = \frac{1}{2}\int_{V_s} \boldsymbol{\varepsilon}_s^{\mathrm{T}} \boldsymbol{\sigma}_s \, \mathrm{d}V_s = \frac{1}{2}\int_{V_s} \mathbf{q}_s^{\mathrm{T}} \mathbf{B}^{\mathrm{T}} \mathbf{C}_s \mathbf{B} \, \mathbf{q}_s \, \mathrm{d}V_s \tag{8}$$

$$\begin{aligned} (U_p)_k &= \sum_{k=1}^{n} \frac{1}{2}\left\{ \int_{V_{p_k}} \boldsymbol{\varepsilon}_{p_k}^{\mathrm{T}} \boldsymbol{\sigma}_{p_k} \mathrm{d}V_{p_k} - \int_{V_{p_k}} \boldsymbol{\varepsilon}_{p_k}^{\mathrm{T}} \mathbf{e}^{\mathrm{T}} \mathbf{E} \, \mathrm{d}V_{p_k} \right\} \\ &= \sum_{k=1}^{n} \frac{1}{2}\left\{ \int_{V_{p_k}} \mathbf{q}_{p_k}^{\mathrm{T}} \mathbf{B}^{\mathrm{T}} \mathbf{C}_{p_k} \mathbf{B} \, \mathbf{q}_{p_k} \mathrm{d}V_{p_k} - \int_{V_{p_k}} \boldsymbol{\varepsilon}_{p_k}^{\mathrm{T}} \mathbf{e}^{\mathrm{T}} \mathbf{E} \, \mathrm{d}V_{p_k} \right\} \end{aligned} \tag{9}$$

Here, $\mathbf{C}$ and $\mathbf{B}$ matrices are the constitutive and differential operator matrices that defines the stress-strain ($\boldsymbol{\sigma} = \mathbf{C}\,\boldsymbol{\epsilon}$) and strain-deformation ($\boldsymbol{\epsilon} = \mathbf{B}\,\mathbf{q}$) relations, $\mathbf{e}$ and $\mathbf{E}$ vectors represent the piezoelectric constants and the electric field, respectively. The details of the constitutive equations for the host panel and the piezoelectric patches are given in Appendix A.

Next, the electrical energy can be written using the electro-elastic relations as

$$W_{ie} = \sum_{k=1}^{n} \frac{1}{2}\int_{V_{p_k}} \mathbf{E}^{\mathrm{T}} \mathbf{D} \, \mathrm{d}V_{p_k} = \sum_{k=1}^{n} \frac{1}{2}\left\{ \int_{V_{p_k}} \mathbf{E}^{\mathrm{T}} \mathbf{e}\, \boldsymbol{\varepsilon}_{p_k} \mathrm{d}V_{p_k} + \int_{V_{p_k}} \mathbf{E}^{\mathrm{T}} \varepsilon^S \mathbf{E} \, \mathrm{d}V_{p_k} \right\} \tag{10}$$

where $\mathbf{D}$ is the electric displacements, $\varepsilon^S$ represent the dielectric permittivity.

Finally, the work done by non-conservative forces can be written as

$$W_{nc} = \frac{1}{2}\int_V \mathbf{f}^{\mathrm{T}}\mathbf{q}\,\mathrm{d}V \tag{11}$$

where $\mathbf{f} = \{\mathbf{f}_{u_0};\, \mathbf{f}_{v_0};\, \mathbf{f}_{w_0};\, \mathbf{f}_{\phi_x};\, \mathbf{f}_{\phi_y}\}$ is the non-conservative force vector.

Inserting the energy terms to the Hamilton's principle yields the BVP. Spectral Chebyshev approach [31, 44] is used to numerically solve this BVP. In this approach, first the domains (*i.e.* the deflections) of the host panel and the piezo-patches are discretized using Gauss-Lobatto sampling to minimize the effect of Runge's phenomenon and improve the computational efficiency simultaneously. Then, the deflection vectors are expressed as a series of double expansion of Chebyshev polynomials of the first kind. To calculate the derivative and integral operations in the BVP, differentiation and inner product matrices that are based on Chebyshev polynomials are derived. The details of the two dimensional spectral Chebyshev approach is given in Appendix B.

Note that, by performing the integral operation along the $z$ direction analytically, the volume integrals can be transformed into area integrals. The integral limits along the $z$ direction are $(z_{l_s}, z_{u_s}) = (-h_s/2, h_s/2)$ for the host structure and $(z_{l_p}, z_{u_p}) = (h_s/2, h_s/2 + h_p)$ or $(-h_s/2 - h_p, -h_s/2)$ for the top or bottom piezoelectric patches, respectively. Therefore, the governing differential equations for the electro-mechanical behavior can be derived in matrix form as:

$$\underbrace{\begin{bmatrix} \mathbf{M}_s & \mathbf{0} & \dots & \dots \\ \mathbf{0} & \mathbf{M}_{p_1} & \dots & \dots \\ \vdots & \dots & \ddots & \mathbf{0} \\ \dots & \dots & \mathbf{0} & \mathbf{M}_{p_n} \end{bmatrix}}_{\mathbf{M}} \begin{bmatrix} \ddot{\mathbf{q}}_s \\ \ddot{\mathbf{q}}_{p_1} \\ \vdots \\ \ddot{\mathbf{q}}_{p_n} \end{bmatrix} + \underbrace{\begin{bmatrix} \mathbf{K}_s & \mathbf{0} & \dots & \dots \\ \mathbf{0} & \mathbf{K}_{p_1} & \dots & \dots \\ \vdots & \dots & \ddots & \mathbf{0} \\ \dots & \dots & \mathbf{0} & \mathbf{K}_{p_n} \end{bmatrix}}_{\mathbf{K}} \begin{bmatrix} \mathbf{q}_s \\ \mathbf{q}_{p_1} \\ \vdots \\ \mathbf{q}_{p_n} \end{bmatrix} - \begin{bmatrix} \mathbf{0} \\ \boldsymbol{\theta}_1 \\ \dots \\ \boldsymbol{\theta}_n \end{bmatrix} v = \begin{bmatrix} \mathbf{f}_s \\ \mathbf{f}_{p_1} \\ \vdots \\ \mathbf{f}_{p_n} \end{bmatrix} \tag{12}$$

Here, $\mathbf{M}$ and $\mathbf{K}$ are the global mass and stiffness matrices of the structure, $\boldsymbol{\theta}$ is the electromechanical coupling vector, and $v$ is the voltage (note that for the parallel connection, the voltage is the same and equal to $v$ for all piezo-patches). The explicit expressions for the system matrices and the electromechanical coupling vector are given in Appendix C.

Similarly, the electrical circuit differential equation for multiple piezo-patch case can be obtained as:

$$\sum_{i=1}^{n} \boldsymbol{\theta}_i^{\mathrm{T}}\, \mathbf{q}_{p_i} + \sum_{i=1}^{n} c_{p_i}\, \dot{v} + Y\, v = 0 \tag{13}$$

where $c_{p_i}$ is the individual piezoelectric patch capacitance and $Y$ is the impedance.

Note that the governing equation defined by Eq. (12) is not structurally coupled. Component mode synthesis approach is used to couple the host panel and piezo-patch dynamics and furthermore to impose the essential boundary conditions if necessary. Following this approach, the coupling equations and boundary condition equations can be expressed as

$$\begin{bmatrix} \boldsymbol{\beta}_{s-p} \\ \boldsymbol{\beta}_{BC} \end{bmatrix} \begin{bmatrix} \mathbf{q}_s \\ \mathbf{q}_{p_1} \\ \vdots \\ \mathbf{q}_{p_n} \end{bmatrix} = \boldsymbol{\beta}\boldsymbol{q}_T = \mathbf{0} \tag{14}$$

Here, $\boldsymbol{\beta}_{s-p}$ and $\boldsymbol{\beta}_{BC}$ matrices include the coupling equations of host panel and piezo-patches, and boundary equations for the host panel, respectively. The critical point here is that since both the host panel and the piezo-patches are sampled individually using Gauss-Lobatto discretization to increase the computational

efficiency, the sampling points of the structures may not coincide. To overcome this issue, the host panel is resampled using the backward and forward transformation matrices (following the formulation given in Appendix D) to include the sampling points of the piezo-patches. Thus, the compatibility equations at the connection boundaries of the host panel and the piezo-patches can be written easily by equating the degrees of freedom (DOFs) at the coinciding sampling points as follows

$$\begin{bmatrix} \mathbf{A}_{s_1}^* & \mathbf{A}_{p_1} & 0 & \dots & \dots \\ \mathbf{A}_{s_2}^* & 0 & \mathbf{A}_{p_2} & 0 & \vdots \\ \vdots & \vdots & \vdots & \ddots & 0 \\ \mathbf{A}_{s_n}^* & 0 & \dots & 0 & \mathbf{A}_{p_n} \end{bmatrix} \begin{Bmatrix} \mathbf{q}_s^* \\ \mathbf{q}_{p_1} \\ \vdots \\ \mathbf{q}_{p_n} \end{Bmatrix} = \mathbf{0} \tag{15}$$

where $\mathbf{q}_s^*$ represents the resampled host panel deformations, $\mathbf{A}_s^*$ and $\mathbf{A}_p$ are the coupling matrices (whose elements are 1, -1, or 0), and the superscript $^*$ denotes the coupling equations corresponding to the resampled host panel. Since, the relationship between the original sampling points and the refined sampling points of the host panel can be written as $\mathbf{q}_s^* = \mathbf{\Gamma}_{B_s}^* \mathbf{\Gamma}_{F_s} \mathbf{q}_s$, the coupling matrix, $\boldsymbol{\beta}_{s-p}$ becomes

$$\boldsymbol{\beta}_{s-p}\, \mathbf{q}_T = \begin{bmatrix} \mathbf{A}_s & \mathbf{A}_p \end{bmatrix} \begin{Bmatrix} \mathbf{q}_s \\ \mathbf{q}_p \end{Bmatrix} = \begin{bmatrix} \mathbf{A}_{s_1} & \mathbf{A}_{p_1} & 0 & \dots & \dots \\ \mathbf{A}_{s_2} & 0 & \mathbf{A}_{p_2} & 0 & \vdots \\ \vdots & \vdots & \vdots & \ddots & 0 \\ \mathbf{A}_{s_n} & 0 & \dots & 0 & \mathbf{A}_{p_n} \end{bmatrix} \begin{Bmatrix} \mathbf{q}_s \\ \mathbf{q}_{p_1} \\ \vdots \\ \mathbf{q}_{p_n} \end{Bmatrix} = \mathbf{0}, \quad \text{where} \quad \mathbf{A}_{s_i} = \mathbf{A}_{s_i}^* \mathbf{\Gamma}_{B_s}^* \mathbf{\Gamma}_{F_s} \tag{16}$$

Then, following the basis recombination approach, the projection matrix, $\mathbf{P}$ that defines a coordinate transformation as $\mathbf{q}_T = \mathbf{P}\mathbf{q}_d$ can be obtained where the particular $\mathbf{q}_d$ satisfies the governing equations. The size of the $\mathbf{P}$ matrix is $N_T \times (N_T - M)$ where $N_T$ is the total number of DOFs and $M$ is the number of rows of $\boldsymbol{\beta}$ matrix (*i.e.*, the number of equations in the $\boldsymbol{\beta}$ matrix).

Based on the linear system assumption, assuming a harmonic excitation as $\mathbf{f} = \bar{\mathbf{f}}_o\, e^{i\omega t}$ and imposing the effects of coupling and boundary condition matrices to the BVP, Eqs. (12) and (13) yield harmonic deflection and voltage vectors as $\mathbf{q}_d = \bar{\mathbf{q}}_{d_o}\, e^{i\omega t}$ and $v = \bar{v}_o\, e^{i\omega t}$. For instance, the harmonic and voltage vectors for the case of parallel connection can be derived as

$$\bar{\mathbf{q}}_{d_o} = \left\{ -\omega^2 \mathbb{M} + \mathbb{K} - \left( \frac{j\omega}{j\omega \sum_{i=1}^{N} c_{p_i} + Y} \right) \mathbf{P}^{\mathrm{T}} \begin{bmatrix} \mathbf{0} \\ \boldsymbol{\theta}_1 \\ \dots \\ \boldsymbol{\theta}_n \end{bmatrix} \begin{bmatrix} \boldsymbol{\theta}_1^{\mathrm{T}} & \dots & \boldsymbol{\theta}_n^{\mathrm{T}} \end{bmatrix} \begin{bmatrix} \mathbf{A}_p^{-1} \mathbf{A}_s & \mathbf{0} \end{bmatrix} \mathbf{P} \right\}^{-1} \mathbf{P}^{\mathrm{T}} \overline{\mathbf{F}} \tag{17}$$

$$\bar{v}_o = \left( \frac{-j\omega}{j\omega \sum_{i=1}^{N} c_{p_i} + Y} \right) \begin{bmatrix} \boldsymbol{\theta}_1^{\mathrm{T}} & \boldsymbol{\theta}_2^{\mathrm{T}} & \dots & \boldsymbol{\theta}_n^{\mathrm{T}} \end{bmatrix} \begin{bmatrix} \mathbf{A}_p^{-1} \mathbf{A}_s & \mathbf{0} \end{bmatrix} \mathbf{P} \bar{\mathbf{q}}_{d_o} \tag{18}$$

where

$$\mathbb{M} = \mathbf{P}^{\mathrm{T}} \mathbf{M} \mathbf{P} \quad \text{and} \quad \mathbb{K} = \mathbf{P}^{\mathrm{T}} \mathbf{K} \mathbf{P} \tag{19}$$

## 3. Model validation

This section presents four case studies using the presented modeling approach described in Section 2: cases (i) and (ii) one piezo-patch on a straight and curved FGM panel, respectively, and cases (iii) and (iv) four piezo-patches on a straight and curved FGM panel, respectively. The geometries of the base panel and the

piezo-patches are illustrated in Fig. 2 and listed in Table 1. In the one-patch case, a piezo-patch size of $300 \times 300$ mm is used; whereas in the four-patch case, the piezo-patch in Fig. 2(a) is divided into four equal parts where the gap between the piezo patches is 6 mm both along the $x$ and $y$ directions. The constituent materials in the FGM panel are aluminum and magnesium. The material variation is assumed to be along $x$ and $y$ directions and the power-law indices ($p$ and $q$) are set to 1. The material properties of the constituent materials and the piezoelectric material are listed in Table 2.

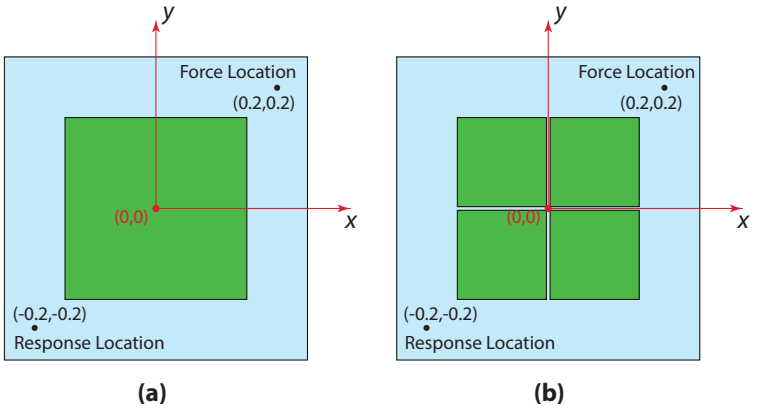


Figure 2: Schematic of the validation case studies: **(a)** one-patch configuration, **(b)** four-patch configuration.

Table 1: Geometric properties of host (FGM) panel and piezoelectric patches

| Property | Base Panel | Piezo-patches | |
|---|---|---|---|
| | | one patch | four patch |
| length ($a_s$ or $a_p$) [mm] | 500 | 300 | 147 |
| width ($b_s$ or $b_p$) [mm] | 500 | 300 | 147 |
| height ($h_s$ or $h_p$) [mm] | 2 | 0.2 | 0.2 |
| curvature ($a_s/r_2$, $b_s/r_1$) | straight: (0,0) or curved: (0.05, 0.05) | | |

Table 2: Material properties of host (FGM) panel and piezoelectric patches

| Property | Aluminum | Magnesium | PZT-5A |
|---|---|---|---|
| Young Modulus [GPa] | 69 | 45 | 61 |
| shear correction factor | $\pi/\sqrt{12}$ | $\pi/\sqrt{12}$ | $\pi/\sqrt{12}$ |
| mass density [kg/m3] | 2700 | 1770 | 7750 |
| Poisson's ratio | 0.33 | 0.33 | 0.35 |
| piezoelectric constant [C/m2] | - | - | -190 |
| permittivity constant [nF/m] | - | - | 9.57 |

Prior to validation, the stability and convergence characteristics of the presented solution approach is demonstrated. Furthermore, the required polynomial numbers along the $x$ and $y$ directions for the host panel and piezo-patches need to be determined since the accuracy of the solution depends on the number of polynomials. Note that, in the case studies, host panel and piezo-patch geometries are selected to be square (however, there is no geometry limitation of the presented solution technique); thus the polynomial numbers along each direction are set equal to each other ($N = N_x = N_y$). In this convergence analysis, the polynomial numbers are incrementally increased both for host panel and piezo-patches and the corresponding natural frequency values are calculated. To assess the level of convergence, the results are compared to a reference

case where the results are obtained using large polynomial numbers ($N_s = 50$ and $N_p = 30$). Tables 3 and 4 list the first ten natural frequency values that are obtained for different polynomial values, and the percent differences with the reference case.

Table 3: Convergence of the first ten natural frequencies for one piezo-patch on a fully-constrained straight FGM panel.

| Modes | $N_s - N_p = 11 - 7$ | | $N_s - N_p = 15 - 9$ | | $N_s - N_p = 31 - 11$ | | $N_s - N_p = 45 - 19$ | | $N_s - N_p = 50 - 30$ |
|---|---|---|---|---|---|---|---|---|---|
| | (Hz) | Diff. (%) | (Hz) | Diff. (%) | (Hz) | Diff. (%) | (Hz) | Diff. (%) | (Reference Case) |
| 1 | 64.56 | 0.08 | 64.52 | 0.03 | 64.50 | 0.01 | 64.50 | 0.00 | 64.50 |
| 2 | 138.78 | 0.37 | 138.60 | 0.25 | 138.34 | 0.06 | 138.27 | 0.01 | 138.25 |
| 3 | 138.78 | 0.37 | 138.60 | 0.25 | 138.34 | 0.06 | 138.27 | 0.01 | 138.25 |
| 4 | 206.46 | 0.35 | 206.26 | 0.26 | 205.86 | 0.07 | 205.74 | 0.01 | 205.72 |
| 5 | 255.75 | 0.66 | 255.32 | 0.51 | 254.33 | 0.12 | 254.08 | 0.02 | 254.02 |
| 6 | 259.66 | 0.55 | 259.26 | 0.41 | 258.45 | 0.10 | 258.24 | 0.02 | 258.19 |
| 7 | 322.81 | 0.49 | 322.33 | 0.36 | 321.46 | 0.09 | 321.24 | 0.02 | 321.18 |
| 8 | 322.81 | 0.49 | 322.33 | 0.36 | 321.46 | 0.09 | 321.24 | 0.02 | 321.18 |
| 9 | 438.34 | 5.24 | 418.10 | 0.40 | 416.69 | 0.07 | 416.50 | 0.02 | 416.42 |
| 10 | 458.90 | 10.18 | 418.10 | 0.40 | 416.69 | 0.07 | 416.50 | 0.02 | 416.42 |

Table 4: Convergence of the first ten natural frequencies for four piezo-patches on a fully-constrained straight FGM panel.

| Modes | $N_s - N_p = 11 - 5$ | | $N_s - N_p = 15 - 7$ | | $N_s - N_p = 31 - 11$ | | $N_s - N_p = 45 - 13$ | | $N_s - N_p = 50 - 30$ |
|---|---|---|---|---|---|---|---|---|---|
| | (Hz) | Diff. (%) | (Hz) | Diff. (%) | (Hz) | Diff. (%) | (Hz) | Diff. (%) | (Reference Case) |
| 1 | 64.87 | 0.11 | 64.84 | 0.09 | 64.81 | 0.04 | 64.79 | 0.02 | 64.78 |
| 2 | 139.04 | 0.45 | 138.68 | 0.22 | 138.47 | 0.06 | 138.41 | 0.02 | 138.38 |
| 3 | 139.04 | 0.45 | 138.68 | 0.21 | 138.47 | 0.05 | 138.41 | 0.01 | 138.39 |
| 4 | 206.17 | 0.42 | 205.73 | 0.22 | 205.41 | 0.06 | 205.31 | 0.01 | 205.28 |
| 5 | 260.86 | 2.63 | 255.06 | 0.38 | 254.46 | 0.14 | 254.17 | 0.03 | 254.10 |
| 6 | 265.01 | 2.61 | 259.06 | 0.33 | 258.55 | 0.13 | 258.28 | 0.02 | 258.22 |
| 7 | 326.24 | 1.61 | 321.92 | 0.28 | 321.34 | 0.10 | 321.07 | 0.02 | 321.02 |
| 8 | 326.24 | 1.61 | 321.92 | 0.28 | 321.34 | 0.10 | 321.07 | 0.02 | 321.02 |
| 9 | 427.33 | 2.60 | 417.85 | 0.34 | 416.74 | 0.07 | 416.51 | 0.02 | 416.43 |
| 10 | 427.33 | 2.60 | 417.85 | 0.34 | 416.74 | 0.07 | 416.51 | 0.02 | 416.43 |

It is clearly shown that the presented solution approach converges very fast as the number of polynomials are increased. The selection of the required polynomial numbers are performed based on the individual modes' error. To have differences less than 0.1% in the first ten modes, the polynomial numbers ($N_s - N_p$) are selected as 45-19 and 45-13 for one piezo-patch and four piezo-patches cases, respectively.

Next, the modal analysis and harmonic analysis results (natural frequencies, structural and electromechanical FRFs) of the presented approach are compared to those obtained using a commercial finite element software (COMSOL $v5.5$). To calculate the FRFs, an excitation force is applied at $(x, y) = (0.2, 0.2)$ along the $z$ direction and the response is measured at $(x, y) = (-0.2, -0.2)$ along $z$ direction. Note that a similar convergence analysis is performed for the FE analysis to determine the sufficient element number. Since the shell elements do not allow to define the top and bottom electrodes, FE models are constructed using solid elements.

In the validations analyses, first, the predicted natural frequencies for cases (i-iv) are compared to the FE results (see Table 5). As shown, the predicted natural frequencies using presented spectral approach and FE analyses are in excellent agreement; the maximum and average percentage differences are calculated as 0.28 % and 0.12 % respectively. Secondly, displacement and voltage FRFs are calculated using Eqs. (17) and (18) to validate the electromechanical response of the system. Figure 3 shows the structural and voltage FRF comparisons for cases (i-iv) assuming open circuit (R=$10^9\Omega$) condition. As shown, the predicted FRFs are matching accurately to the FRFs calculated using FE approach.

Table 5: Comparison of first ten natural frequencies (in Hz) predicted using the presented solution approach and FE analysis for **(i-ii)** one piezo-patch on a straight and curved FGM panel and **(iii-iv)** four piezo-patches on a straight and curved FGM panel. For each case, the panel is fully-constrained.

| | one piezo-patch | | | | | | four piezo-patches | | | | | |
|---|---|---|---|---|---|---|---|---|---|---|---|---|
| | straight FGM panel | | | curved FGM panel | | | straight FGM panel | | | curved FGM panel | | |
| | Present | FE | Diff. (%) | Present | FE | Diff. (%) | Present | FE | Diff. (%) | Present | FE | Diff. (%) |
| 1 | 64.50 | 64.54 | 0.05 | 114.96 | 114.83 | 0.12 | 64.81 | 64.66 | 0.23 | 115.86 | 115.55 | 0.27 |
| 2 | 138.32 | 138.33 | 0.01 | 157.77 | 157.77 | 0.00 | 138.47 | 138.40 | 0.05 | 158.00 | 157.86 | 0.09 |
| 3 | 138.32 | 138.34 | 0.01 | 157.77 | 157.79 | 0.01 | 138.47 | 138.42 | 0.04 | 158.00 | 157.89 | 0.07 |
| 4 | 205.83 | 205.86 | 0.01 | 220.09 | 220.16 | 0.03 | 205.40 | 205.39 | 0.01 | 219.57 | 219.48 | 0.04 |
| 5 | 254.22 | 254.30 | 0.03 | 265.19 | 265.36 | 0.06 | 254.37 | 253.71 | 0.26 | 265.39 | 264.70 | 0.26 |
| 6 | 258.35 | 258.52 | 0.07 | 272.52 | 272.78 | 0.09 | 258.47 | 257.75 | 0.28 | 272.61 | 271.84 | 0.28 |
| 7 | 321.38 | 321.64 | 0.08 | 330.92 | 331.30 | 0.11 | 321.26 | 320.88 | 0.12 | 330.81 | 330.35 | 0.14 |
| 8 | 321.38 | 321.67 | 0.09 | 330.92 | 331.35 | 0.13 | 321.26 | 320.91 | 0.11 | 330.81 | 330.39 | 0.13 |
| 9 | 416.69 | 417.45 | 0.18 | 423.77 | 424.73 | 0.23 | 416.75 | 417.38 | 0.15 | 423.77 | 424.33 | 0.13 |
| 10 | 416.69 | 417.49 | 0.19 | 423.77 | 424.77 | 0.24 | 416.75 | 417.42 | 0.16 | 423.77 | 424.42 | 0.15 |

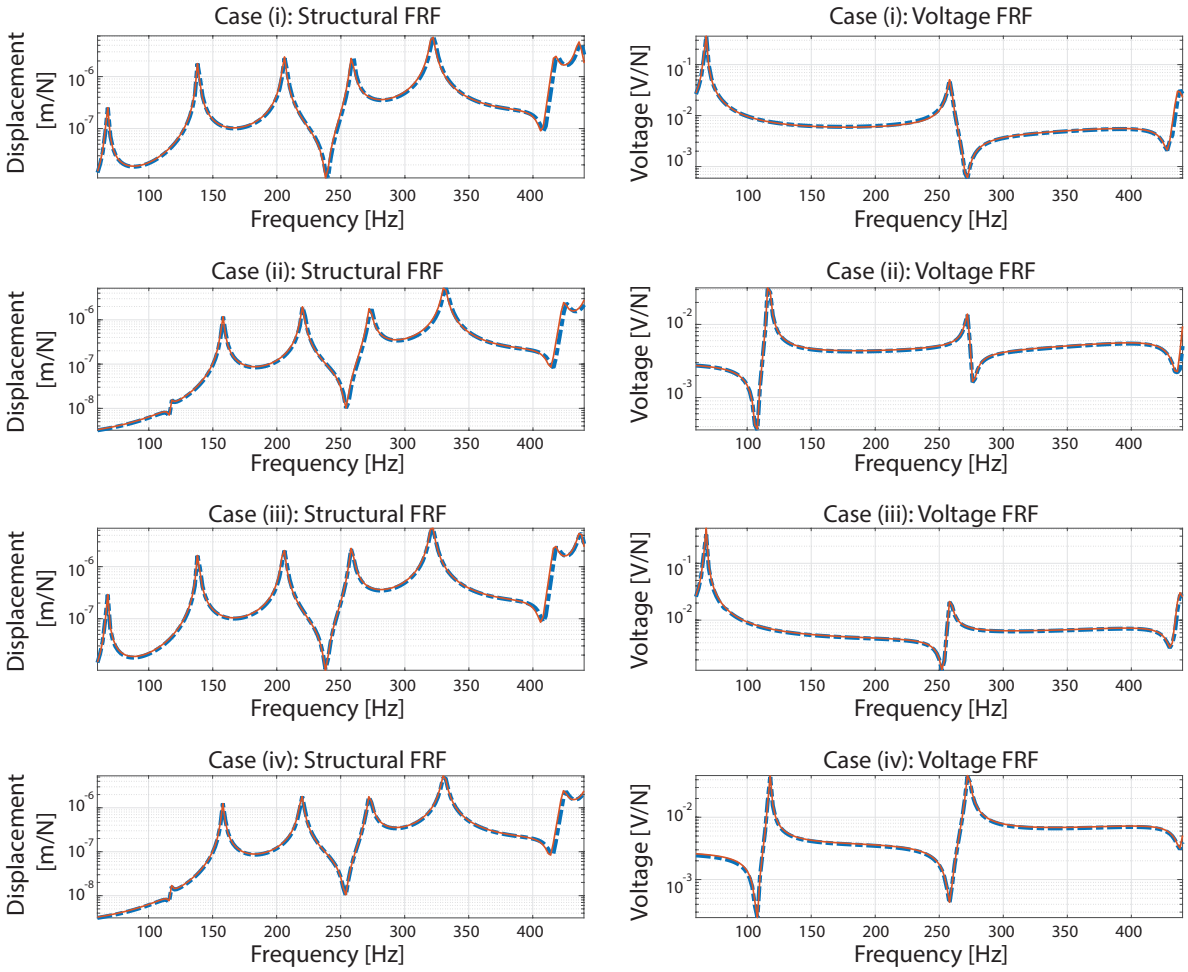


Figure 3: Comparison of structural and open circuit voltage FRFs for cases (i)-(iv). Cases (i) and (ii) correspond to one piezo-patch configuration on a straight and curved FGM panel, respectively. Similarly, cases (iii) and (iv) correspond to four piezo-patches configuration on a straight and curved FGM panel, respectively. The solid red lines are the results predicted using the presented solution approach, and the dashed blue lines are FE results.

## 4. Design of FGM panel

### *4.1. Effect of material gradation on electromechanical behavior*

Depending on the constituent material properties of the FGM panel, the compliance of the structure varies spatially which significantly affects the performance of piezo-patches. Thus, in this section, the effect of material variation along $x$ and $y$ directions on voltage ($V$) and power ($P$) output of piezo-patches is investigated. Although this investigation can be performed for multiple piezo-patches, to demonstrate the material variation effects clearly, only single surface-integrated piezo-patch cases are considered. Thus, using the geometry of case (ii) described in Sec. 3 (curved FGM panel having one piezo-patch), power law indices defined in Eq. (1) are varied between 0 and 10 with 0.1 resolution. Figure 4 shows the variation of fundamental natural frequency, open circuit voltage output, and power output with a resistor value of $R = 10^4\,\Omega$ for one piezo-patch attached on a curved FGM panel with respect to a homogeneous panel (*i.e.* aluminum panel). It is also observed that, when the lighter material amount is increased, the fundamental frequency changes slightly (around 4%); however the voltage and power output can increase significantly.

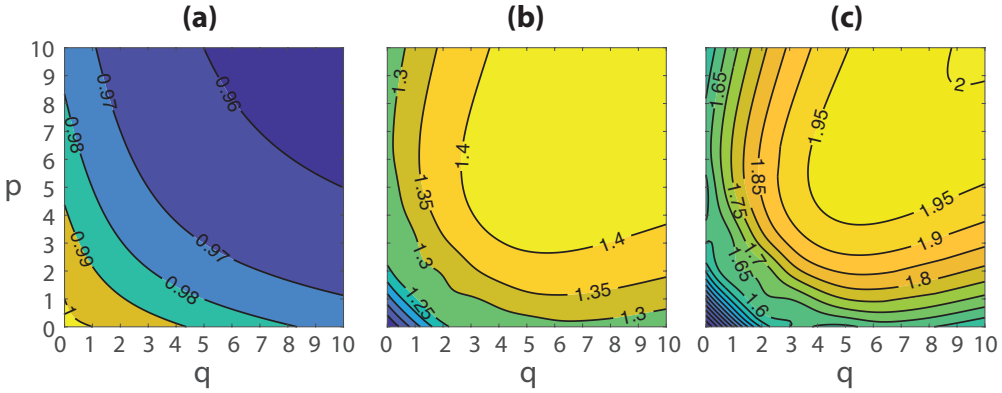


Figure 4: Effect of power law indices on fundamental natural frequency, open circuit voltage output (amplitude), and power output (amplitude): **(a)** $\omega_o/\omega_{o_{\mathrm{REF}}}$, **(b)** $V_{\mathrm{OC}}/V_{\mathrm{OC}_{\mathrm{REF}}}$, and **(c)** $P/P_{\mathrm{REF}}$.

Note that in the analyses presented in Fig. 4, the power law function given in Eq. (1) leads to a symmetric material distribution. However, it is also possible to create asymmetric material gradation using a four-parameter power law distribution (for each direction) using the following equation [45]:

$$V_{\mathrm{mat}_1}(x,y) = \left[1 - \alpha_x\left(\frac{1}{2} + \frac{x}{a_s}\right) + \beta_x\left(\frac{1}{2} + \frac{x}{a_s}\right)^{\gamma_x}\right]^p \left[1 - \alpha_y\left(\frac{1}{2} + \frac{y}{b_s}\right) + \beta_y\left(\frac{1}{2} + \frac{y}{b_s}\right)^{\gamma_y}\right]^q \tag{20}$$

where $\alpha$, $\beta$, and $\gamma$ dictate the material variation profile along $x$ and $y$ directions together with the power-law indices ($p$ and $q$). To further illustrate the influence of the material variation on the power output of the piezo-patches, we performed several analyses using various values of the four-parameters (see Table 6) in Eq. (20) for a fully-constrained straight and curved FGM panels having the geometry properties described in cases (i) and (ii) in Sec. 3. For simplicity, the material variation profiles along $x$ and $y$ directions are assumed to be identical (*i.e.* $\alpha_x = \alpha_y$, $\beta_x = \beta_y$, and $\gamma_x = \gamma_y$), and the power law indices are swept from 0 to 5. The values of power law indices that leads to the maximum power output density for each option is plotted in Fig. 5. As seen in this figure, the power output density (power/volume of piezoelectric patch) can be significantly increased (up to 84% and 102% for straight and curved FGM panels, respectively) leveraging the spatial material distribution of the FGM panel.

Table 6: Material variation parameters for selected distribution models

| Option | $\alpha_x = \alpha_y$ | $\beta_x = \beta_y$ | $\gamma_x = \gamma_y$ |
|---|---|---|---|
| 1 | 1 | 0 | - |
| 2 | 1 | 0.5 | 2 |
| 3 | 1 | 1 | 2 |
| 4 | 1 | 1 | 4 |
| 5 | 0.8 | 0.2 | 3 |

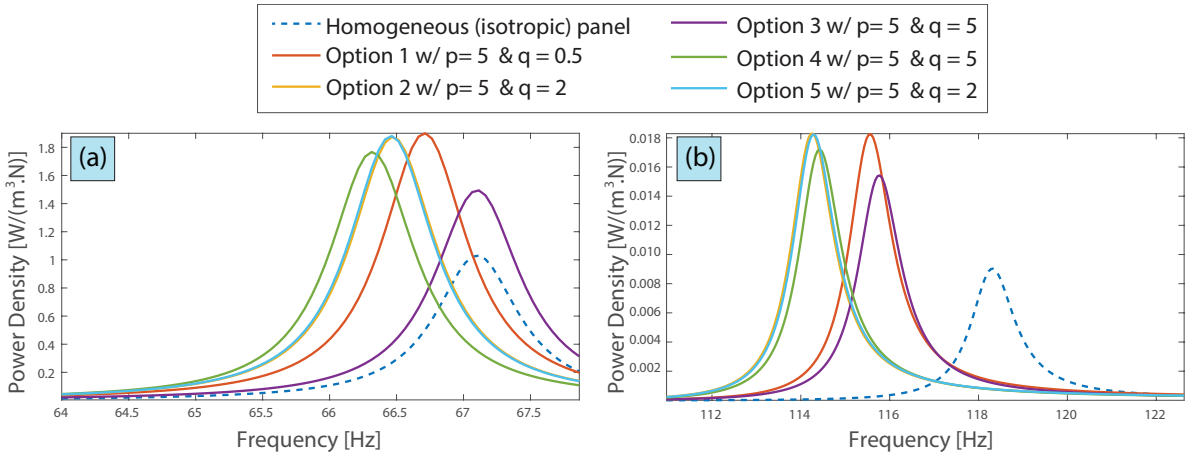


Figure 5: Effect of material distribution on power output density of a fully-constrained **(a)** straight and **(b)** curved ($a_s/r_2 = b_s/r_1 = 0.05$) panel.

### *4.2. Optimization of material gradation to maximize the harvested power density*

As discussed in Sec. 4.1, it is evident that FGM panel can produce more voltage and power compared to homogenous (isotropic) panel. However, note that the peak location changes due to the change in spatial stiffness of the panel. In other words, as the volumetric ratio of the lighter and softer material increases, the fundamental natural frequency of the panel decreases. Despite that, it is possible to increase the power (or voltage) output of the piezo-patches while setting the peak location at a desired frequency through material and shape/geometry variations (such as the size of the piezo-patches or thickness of the host panel, *etc.*). Therefore, in this case study, an optimization simulation is performed using the genetic algorithm toolbox in MATLAB to maximize the power output density of the piezo-patch. The design variables are selected to be the parameters ($\alpha$, $\beta$, $\gamma$, $p$, and $q$) in Eq. (20) and the size of the square piezo-patch ($a_p = b_p$). Maximizing the power density (power/volume of piezoelectric patch) near the first natural frequency of the isotropic cases ($\pm 0.2\%$) is considered as the objective function. The constraints used in the optimization software are as follows:

$$
\begin{aligned}
&0 \le \alpha \le 1;\;\; 0 \le \beta \le 1;\;\; 0 \le \gamma \le 4;\;\; 0 \le p \le 5;\;\; 0 \le q \le 5 \\
&0 \le \left[1 - \alpha_x\left(\frac{1}{2} + \frac{x}{a_s}\right) + \beta_x\left(\frac{1}{2} + \frac{x}{a_s}\right)^{\gamma_x}\right] \le 1;\;\; \forall x \\
&0 \le \left[1 - \alpha_y\left(\frac{1}{2} + \frac{y}{a_s}\right) + \beta_y\left(\frac{1}{2} + \frac{y}{a_s}\right)^{\gamma_y}\right] \le 1;\;\; \forall y \\
&270\,mm \le a_p = b_p \le 330\,mm
\end{aligned}
\tag{21}
$$

In the analyses, we used the geometries of cases (i) and (ii) defined in Sec. 3 for a fully-constrained straight and curved FGM panel, respectively. The genetic algorithm results are compared to the homogeneous panel

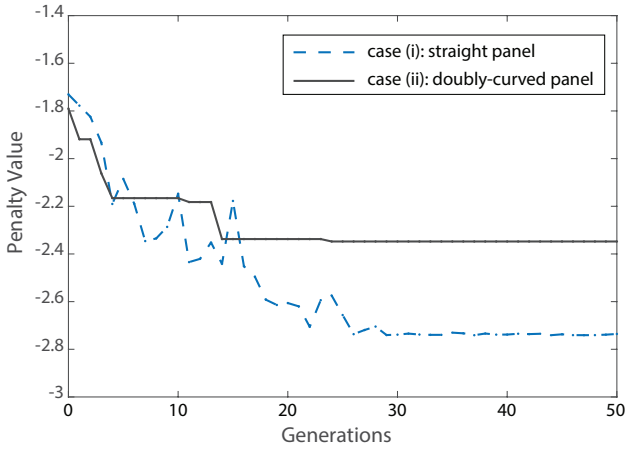


Figure 6: Comparison of penalty values for cases (i) and (ii).

results to assess the improvements in power output density of the piezo-patches. To find the optimal material distribution parameters and the size of the piezo-patch as well as the penalty value, the population size is assumed as 200. Figure 6 shows the comparison of the penalty values for cases (i) and (ii) as function of the generation numbers.

It is seen that after 30 generations the maximum power density converges. The optimal material parameter values and piezo patch sizes are listed in Table 7 and the corresponding power densities at the fundamental frequencies are plotted in Fig. 7 for straight and curved panels. Note that, introducing curvature to the panel, the stiffness is significantly increased leading to smaller deformations compared to straight/flat panels. As a result, the harvested voltage or power levels are smaller compared to straight panels. As observed in Table 7 and Fig. 7, significant increases in power and voltage output can be achieved through optimizing the material and shape/geometry variation both for straight and curved FGM panels. For instance, 174% and 134% improvements can be obtained for cases (i) and (ii) compared to the maximum power density values obtained for homogeneous panels.

Table 7: Optimal parameters for cases A and B

| Case | p | q | $\alpha_x$ | $\alpha_y$ | $\beta_x$ | $\beta_y$ | $\gamma_x$ | $\gamma_y$ | $a_p = b_p$ [mm] | max. power density [W/m$^3$N] | imp. (%) |
|---|---|---|---|---|---|---|---|---|---|---|---|
| (i) | 0 | 0 | - | - | - | - | - | - | 300 | 1.03 | - |
| (i) - optimal | 4 | 4 | 0.5 | 1 | 0.2 | 0.3 | 1 | 4 | 270 | 2.82 | 174 |
| (ii) | 0 | 0 | - | - | - | - | - | - | 300 | $0.903\times10^{-2}$ | - |
| (ii) - optimal | 0 | 4 | - | 0.5 | - | 0.4 | - | 3 | 270 | $2.11\times10^{-2}$ | 134 |

## 5. Conclusion

In this study, we presented a spectral modeling approach to accurately predict the electro-mechanical behavior of (doubly-) curved FGM panels integrated with multiple piezo patches. The governing equations is derived following the Hamilton's principle where the strain and kinetic energies are obtained using FSDT. To impose the material variation, power law distribution is selected and the spatial material properties are predicted using theory of mixtures. Component mode synthesis approach is used to express the compatibility equations. Then basis recombination approach is followed to couple the piezoelectric patches and

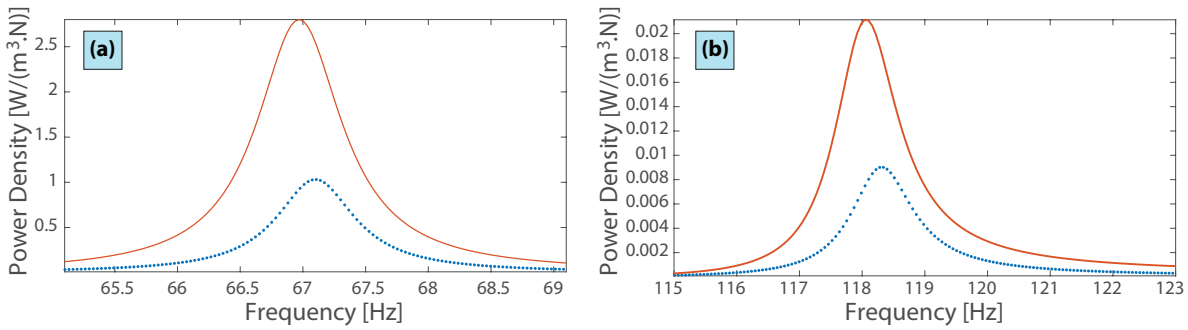


Figure 7: Effect of material distribution on power output density of a fully-constrained **(a)** straight and **(b)** curved ($a_s/r_2 = b_s/r_1 = 0.05$) panel. The dotted (blue) and solid (red) lines represent the homogenous (isotropic) panel with $a_s = b_s = 300mm$ and optimized FGM panel and piezo-patch size (see Table 7 for the optimized values for the parameters of four-parameter power law distribution equation and size of the square piezo-patch).

the host structure. The numerical solution of the governing equations is performed via spectral Chebyshev approach.

To demonstrate the accuracy of the solution approach in predicting the natural frequencies and structural/voltage frequency response functions, several case studies are performed for straight and curved FGM panels with single/multiple piezo-patch configurations. The predicted results are validated comparing them to those obtained using COMSOL. It is shown that the results are in excellent agreement both for the predicted natural frequencies and voltage/displacement FRFs.

Next, it is shown that the material variation in the FGM panel significantly affect the voltage and power output of piezo-patches. However, depending on the material properties of the constituent materials, the peak location of the voltage FRFs may change. Therefore, in the last case study, it is demonstrated that the developed design framework can be utilized to maximize the power/voltage output of the piezo-patches through material and geometry/shape variations. Based on the investigated case studies, improvements (in terms of the maximum power density) up to 134% can be achieved using the FGM panels compared to the homogenoues (isotropic) ones. This result highlights the importance of considering material variation parameters and geometry/shape parameters as design variables to maximize the power and voltage output at any desired/targeted frequency.

## Appendix A. Constitutive equations

The constitutive matrix for the host panel defines the relationship between the stresses and the strains ($\boldsymbol{\sigma} = \mathbf{C}\,\boldsymbol{\epsilon}$) and can be expressed in terms of Lamé parameters ($\lambda$ and $\mu$) as

$$\mathbf{C}_s = \begin{bmatrix} \lambda & \nu\lambda & 0 & 0 & 0 \\ \nu\lambda & \lambda & 0 & 0 & 0 \\ 0 & 0 & \mu & 0 & 0 \\ 0 & 0 & 0 & k^2\mu & 0 \\ 0 & 0 & 0 & 0 & k^2\mu \end{bmatrix} \tag{A.1}$$

where $\nu$ is the Poisson's ratio and $k$ is the shear correction factor (taken as $\pi/\sqrt{12}$). In the case of piezoelectric patches, the constitutive equations are defined using electro-elastic relations as

$$\begin{bmatrix} \boldsymbol{\sigma} \\ \mathbf{D} \end{bmatrix} = \begin{bmatrix} \mathbf{C}_p^E & -\mathbf{e}^{\mathrm{T}} \\ \mathbf{e} & \epsilon^S \end{bmatrix} \begin{bmatrix} \boldsymbol{\epsilon} \\ \mathbf{E} \end{bmatrix} \tag{A.2}$$

Here, $c_{ij_p}^E$'s (*i.e.* the elements of $\mathbf{C}_p^E$ matrix) are the reduced elastic moduli for piezoelectric patches at constant electric field, $\mathbf{e} = \{\bar{e}_{31}; \bar{e}_{31}; 0; 0; 0\}$ is the vector of piezoelectric constants, $\mathbf{D}$ is the piezoelectric displacement vector and $\mathbf{E}$ is the vector of electric field term.

## Appendix B. Two-dimensional Chebyshev approach

### *Appendix B.1. Chebyshev expansion and domain discretization*

Any function, $f(x)$, can be expressed using Chebyshev polynomials as

$$f(x) = \sum_{k=1}^{N} a_k \mathcal{T}_{k-1}(x) \tag{B.1}$$

Here, $\mathcal{T}$'s are the Chebyshev polynomials of the first kind [46], $a_k$'s are the expansion coefficients, $N$ is the polynomial number. Since, there is a one-to-one mapping between the functions values at the sampling points and the expansion coefficients, it is possible to define a relation between the sampled function's values and the expansion coefficients as

$$\mathbf{a} = \mathbf{\Gamma}_F \, \mathbf{y} \quad \text{or} \quad \mathbf{y} = \mathbf{\Gamma}_B \, \mathbf{a} \tag{B.2}$$

where $\mathbf{\Gamma}_F$ and $\mathbf{\Gamma}_B$ are the $(N \times N)$ forward and backward transformation matrices [47].

However, the deflection terms are functions of both $x$ and $y$ in the derived governing equations given in Eqs. (12) and (13). Thus, after the problem domain is first discretized using Gauss-Lobatto sampling approach, we need to use double-expansion of Chebyshev polynomials as

$$q_{kl} = \sum_{k=1}^{N_x} \sum_{l=1}^{N_y} a_{q_i} \mathcal{T}_{k-1}(x) \mathcal{T}_{l-1}(y), \tag{B.3}$$

Here, $N_x$ and $N_y$ are the polynomial numbers used along $x$ and $y$ directions, respectively. To represent the deflection terms in a vector form, a tensor-to-vector mapping operation ($i = (k-1)N_y + l$) is applied. Thus, after the discretization process, the deflection vector can be written as

$$\mathbf{u}_o = \begin{bmatrix} \mathbb{I} & \mathbb{0} & \mathbb{0} & \mathbb{0} & \mathbb{0} \end{bmatrix} \mathbf{q} = \mathbb{I}_u \, \mathbf{q} \tag{B.4}$$

$$\mathbf{v}_o = \begin{bmatrix} \mathbb{0} & \mathbb{I} & \mathbb{0} & \mathbb{0} & \mathbb{0} \end{bmatrix} \mathbf{q} = \mathbb{I}_v \, \mathbf{q} \tag{B.5}$$

$$\mathbf{w}_o = \begin{bmatrix} \mathbb{0} & \mathbb{0} & \mathbb{I} & \mathbb{0} & \mathbb{0} \end{bmatrix} \mathbf{q} = \mathbb{I}_w \, \mathbf{q} \tag{B.6}$$

$$\boldsymbol{\phi}_x = \begin{bmatrix} \mathbb{0} & \mathbb{0} & \mathbb{0} & \mathbb{I} & \mathbb{0} \end{bmatrix} \mathbf{q} = \mathbb{I}_{\phi_x} \, \mathbf{q} \tag{B.7}$$

$$\boldsymbol{\phi}_y = \begin{bmatrix} \mathbb{0} & \mathbb{0} & \mathbb{0} & \mathbb{0} & \mathbb{I} \end{bmatrix} \mathbf{q} = \mathbb{I}_{\phi_y} \, \mathbf{q} \tag{B.8}$$

where $\mathbb{I}$ and $\mathbb{0}$ are $(N_x N_y \times N_x N_y)$ identity and zero matrices, respectively; and $\mathbb{I}_{q_i}$ is the $(N_x N_y \times 5 N_x N_y)$ operator matrix.

It is possible to derive a similar relationship as given in Eq. (B.2), for the double expansion case given in Eq. (B.3) [48]. Following a similar tensor-to-matrix mapping operation, the transformation matrices that are obtained for each direction can be used to obtain the extended $(N_x N_y \times N_x N_y)$ forward and backward

transformation matrices as

$$\mathbb{\Gamma}_{B_{c_1c_2}} = \Gamma^x_{B_{k_1k_2}} \Gamma^y_{B_{l_1l_2}} \tag{B.9}$$

$$c_1 = (k_1 - 1)N_y + l_1, \quad c_2 = (k_2 - 1)N_y + l_2 \tag{B.10}$$

$$k_1 = 1, \ldots, N_x \quad k_2 = 1, \ldots, N_x \tag{B.11}$$

$$l_1 = 1, \ldots, N_y \quad l_2 = 1, \ldots, N_y \tag{B.12}$$

*Appendix B.2. Differentiation in Chebyshev domain*

The spatial derivative of a function, $f(x)$, can also be expressed by a series expansion of Chebyshev polynomials. We can write a relationship between the coefficients of the original function and its derivative as $\mathbf{b} = \mathbf{D}^x\,\mathbf{a}$, where $\mathbf{b}$ is the coefficient vector for the derivative of the original function and $\mathbf{D}^x$ is the derivative matrix. However, since the problem domain is two-dimensional, following the aforementioned mapping for transformation matrices, extended derivative matrices with respect ot $x$ and $y$ can be obtained as follows

$$\mathbb{D}^x_{c_1c_2} = D^x_{k_1k_2} \quad \text{and} \quad \mathbb{D}^y_{c_1c_2} = D^x_{l_1l_2} \tag{B.13}$$

$$c_1 = (k_1 - 1)N_y + l_1, \quad c_2 = (k_2 - 1)N_y + l_2 \tag{B.14}$$

$$k_1 = 1, \ldots, N_x \quad k_2 = 1, \ldots, N_x \tag{B.15}$$

$$l_1 = 1, \ldots, N_y \quad l_2 = 1, \ldots, N_y \tag{B.16}$$

Note that the derivative matrices defines a relationship between the coefficients of the function and its derivative. Thus, using the extended forward and backward transformation matrices, differentiation matrices ($\mathbf{Q}_x$ and $\mathbf{Q}_y$) that defines the functions values and its derivative at the sampling points can be derived as

$$\mathbf{q}_{,x} = \mathbb{\Gamma}_B \mathbf{b} = \mathbb{\Gamma}_B \mathbb{D}^x \mathbf{a} = \mathbb{\Gamma}_B \mathbb{D}^x \mathbb{\Gamma}_F\, \mathbf{q} = \mathbf{Q}_x\, \mathbf{q} \tag{B.17}$$

$$\mathbf{q}_{,y} = \mathbb{\Gamma}_B \mathbf{b} = \mathbb{\Gamma}_B \mathbb{D}^y \mathbf{a} = \mathbb{\Gamma}_B \mathbb{D}^y \mathbb{\Gamma}_F\, \mathbf{q} = \mathbf{Q}_y\, \mathbf{q} \tag{B.18}$$

Note that the differentiation can be calculated exactly if the function can be expressed exactly using Chebyshev polynomials [47].

*Appendix B.3. Integration in Chebyshev domain*

The integral operation of a function, $f(x)$, is performed using based on the definite integral vector, $\mathbf{v}$, as

$$\int_0^l y(x)\mathrm{d}x = \sum_1^N a_k \int_0^l \mathcal{T}_{k-1}(x)\mathrm{d}x = \mathbf{v}^{\mathrm{T}}\mathbf{a} \tag{B.19}$$

Similar to derivative operation, if the function can be expressed exactly using $N$ Chebyshev polynomials, the integral operation can be computed exactly.

In the case of integral operation that includes multiplication of multiple functions, inner product approach is used. For instance, the integral operations defined in energy equations of host panel includes three functions since the material properties vary spatially; whereas there are two functions in energy equations of piezo-patches (see Section 2.2). Following the inner product matrix approach [47–49], the integral operations can be calculated as

$$\int f(x,y)g(x,y)\mathrm{d}x\mathrm{d}y = \mathbf{f}^{\mathrm{T}}\,\mathbb{V}\,\mathbf{g} \tag{B.20}$$

$$\int r(x,y)f(x,y)g(x,y)\mathrm{d}x\mathrm{d}y = \mathbf{f}^{\mathrm{T}}\,\mathbb{V}^r\,\mathbf{g} \tag{B.21}$$

where $f(x,y)$ and $g(x,y)$ represent the deflection terms, $r(x,y)$ represents the varying material property functions, $\mathbb{V}$ and $\mathbb{V}^r$ are the inner product and weighted inner product matrices, respectively.

## Appendix C. System matrices

Following the spectral Chebyshev approach, the system matrices and the electromechanical coupling vector in Eq. (12) can be derived as:

$$\mathbf{M}_s = \left[ h_s \left( \mathbb{I}_{u_s}^{\mathrm{T}} \mathbb{V}_s^{\rho} \mathbb{I}_{u_s} + \mathbb{I}_{v_s}^{\mathrm{T}} \mathbb{V}_s^{\rho} \mathbb{I}_{v_s} + \mathbb{I}_{w_s}^{\mathrm{T}} \mathbb{V}_s^{\rho} \mathbb{I}_{w_s} \right) + \frac{h_s^3}{12} \left( \mathbb{I}_{\phi_{x_s}}^{\mathrm{T}} \mathbb{V}_s^{\rho} \mathbb{I}_{\phi_{x_s}} + \mathbb{I}_{\phi_{y_s}}^{\mathrm{T}} \mathbb{V}_s^{\rho} \mathbb{I}_{\phi_{y_s}} \right) \right] \tag{C.1}$$

$$\mathbf{K}_s = \mathbf{B}_s^{\mathrm{T}} \mathbb{V}_s \mathbf{C}_{h_s} \mathbf{B}_s \tag{C.2}$$

$$\mathbf{M}_{p_k} = \left\{ 2\rho_p \left[ \left( \frac{h_p^3}{3} + \frac{h_p^2 h_p}{4} + \frac{h_s h_p}{2} \right) \left( \mathbb{I}_{\phi_{x_p}}^{\mathrm{T}} \mathbb{V}_p \mathbb{I}_{\phi_{x_p}} + \mathbb{I}_{\phi_{y_p}}^{\mathrm{T}} \mathbb{V}_p \mathbb{I}_{\phi_{y_p}} \right) + h_p \left( \mathbb{I}_{u_p}^{\mathrm{T}} \mathbb{V}_p \mathbb{I}_{u_p} + \mathbb{I}_{v_p}^{\mathrm{T}} \mathbb{V}_p \mathbb{I}_{v_p} + \mathbb{I}_{w_p}^{\mathrm{T}} \mathbb{V}_p \mathbb{I}_{w_p} \right) \right] \right\}_k \tag{C.3}$$

$$\mathbf{K}_{p_k} = \left( \mathbf{B}_p^{\mathrm{T}} \mathbb{V}_p \mathbf{C}_{h_p} \mathbf{B}_p \right)_k \tag{C.4}$$

$$\boldsymbol{\theta}_k = \left[ \left( \frac{h_p + h_s}{2} \right) \left( \boldsymbol{\varepsilon}_{xx_p}^{\mathrm{T}} \mathbb{V}_p e_{31} + \boldsymbol{\varepsilon}_{yy_p}^{\mathrm{T}} \mathbb{V}_p e_{31} \right) \right]_k \tag{C.5}$$

where $\mathbf{C}_{h_s}$ and $\mathbf{C}_{h_p}$ are the linear elastic constitutive matrices that includes the thickness term, $h$ as a result of the analytical integration along $z$ direction. For instance, for the host panel, the stiffness matrix can be explicitly written as

$$\begin{aligned}
\mathbf{K}_s = h \Bigg\{ & \mathbb{I}_{u_s}^{\mathrm{T}} \mathbf{Q}_{x_s}^{\mathrm{T}} \mathbb{V}_s^{\lambda} \mathbf{Q}_{x_s} \mathbb{I}_{u_s} + \frac{1}{r_1} \mathbb{I}_{u_s}^{\mathrm{T}} \mathbf{Q}_{x_s}^{\mathrm{T}} \mathbb{V}_s^{\lambda} \mathbb{I}_{w_s} + \frac{1}{r_1} \mathbb{I}_{w_s}^{\mathrm{T}} \mathbb{V}_s^{\lambda} \mathbf{Q}_{x_s} \mathbb{I}_{u_s} + \frac{1}{r_1^2} \mathbb{I}_{w_s}^{\mathrm{T}} \mathbb{V}_s^{\lambda} \mathbb{I}_{u_s} + \frac{h^2}{12} \mathbb{I}_{\phi_{x_s}}^{\mathrm{T}} \mathbf{Q}_{x_s}^{\mathrm{T}} \mathbb{V}_s^{\lambda} \mathbf{Q}_{x_s} \mathbb{I}_{\phi_{x_s}} \\
& + \nu \Bigg( \mathbb{I}_{u_s}^{\mathrm{T}} \mathbf{Q}_{x_s}^{\mathrm{T}} \mathbb{V}_s^{\lambda} \mathbf{Q}_{y_s} \mathbb{I}_{v_s} + \frac{1}{r_2} \mathbb{I}_{u_s}^{\mathrm{T}} \mathbf{Q}_{x_s}^{\mathrm{T}} \mathbb{V}_s^{\lambda} \mathbb{I}_{w_s} + \frac{1}{r_2} \mathbb{I}_{w_s}^{\mathrm{T}} \mathbb{V}_s^{\lambda} \mathbf{Q}_{y_s} \mathbb{I}_{v_s} + \frac{1}{r_1 r_2} \mathbb{I}_{w_s}^{\mathrm{T}} \mathbb{V}_s^{\lambda} \mathbb{I}_{w_s} + \frac{h^2}{12} \mathbb{I}_{\phi_{x_s}}^{\mathrm{T}} \mathbf{Q}_{x_s}^{\mathrm{T}} \mathbb{V}_s^{\lambda} \mathbf{Q}_{y_s} \mathbb{I}_{\phi_{y_s}} \\
& + \mathbb{I}_{v_s}^{\mathrm{T}} \mathbf{Q}_{y_s}^{\mathrm{T}} \mathbb{V}_s^{\lambda} \mathbf{Q}_{x_s} \mathbb{I}_{u_s} + \frac{1}{r_1} \mathbb{I}_{v_s}^{\mathrm{T}} \mathbf{Q}_{x_s}^{\mathrm{T}} \mathbb{V}_s^{\lambda} \mathbb{I}_{w_s} + \frac{1}{r_2} \mathbb{I}_{w_s}^{\mathrm{T}} \mathbb{V}_s^{\lambda} \mathbf{Q}_{x_s} \mathbb{I}_{u_s} + \frac{1}{r_1 r_2} \mathbb{I}_{w_s}^{\mathrm{T}} \mathbb{V}_s^{\lambda} \mathbb{I}_{w_s} + \frac{h^2}{12} \mathbb{I}_{\phi_{y_s}}^{\mathrm{T}} \mathbf{Q}_{y_s}^{\mathrm{T}} \mathbb{V}_s^{\lambda} \mathbf{Q}_{x_s} \mathbb{I}_{\phi_{x_s}} \Bigg) \\
& + \mathbb{I}_{v_s}^{\mathrm{T}} \mathbf{Q}_{y_s}^{\mathrm{T}} \mathbb{V}_s^{\lambda} \mathbf{Q}_{y_s} \mathbb{I}_{v_s} + \frac{1}{r_2} \mathbb{I}_{v_s}^{\mathrm{T}} \mathbf{Q}_{y_s}^{\mathrm{T}} \mathbb{V}_s^{\lambda} \mathbb{I}_{w_s} + \frac{1}{r_2} \mathbb{I}_{w_s}^{\mathrm{T}} \mathbb{V}_s^{\lambda} \mathbf{Q}_{y_s} \mathbb{I}_{v_s} + \frac{1}{r_2^2} \mathbb{I}_{w_s}^{\mathrm{T}} \mathbb{V}_s^{\lambda} \mathbb{I}_{w_s} + \frac{h^2}{12} \mathbb{I}_{\phi_{y_s}}^{\mathrm{T}} \mathbf{Q}_{y_s}^{\mathrm{T}} \mathbb{V}_s^{\lambda} \mathbf{Q}_{y_s} \mathbb{I}_{\phi_{y_s}} \\
& + \mathbb{I}_{u_s}^{\mathrm{T}} \mathbf{Q}_{y_s}^{\mathrm{T}} \mathbb{V}_s^{\mu} \mathbf{Q}_{y_s} \mathbb{I}_{u_s} + \mathbb{I}_{u_s}^{\mathrm{T}} \mathbf{Q}_{y_s}^{\mathrm{T}} \mathbb{V}_s^{\mu} \mathbf{Q}_{x_s} \mathbb{I}_{v_s} + \mathbb{I}_{v_s}^{\mathrm{T}} \mathbf{Q}_{x_s}^{\mathrm{T}} \mathbb{V}_s^{\mu} \mathbf{Q}_{y_s} \mathbb{I}_{u_s} + \mathbb{I}_{v_s}^{\mathrm{T}} \mathbf{Q}_{x_s}^{\mathrm{T}} \mathbb{V}_s^{\mu} \mathbf{Q}_{x_s} \mathbb{I}_{v_s} \\
& + \frac{h^2}{12} \left( \mathbb{I}_{\phi_{x_s}}^{\mathrm{T}} \mathbf{Q}_{y_s}^{\mathrm{T}} \mathbb{V}_s^{\mu} \mathbf{Q}_{y_s} \mathbb{I}_{\phi_{x_s}} + \mathbb{I}_{\phi_{x_s}}^{\mathrm{T}} \mathbf{Q}_{y_s}^{\mathrm{T}} \mathbb{V}_s^{\mu} \mathbf{Q}_{x_s} \mathbb{I}_{\phi_{y_s}} + \mathbb{I}_{\phi_{y_s}}^{\mathrm{T}} \mathbf{Q}_{x_s}^{\mathrm{T}} \mathbb{V}_s^{\mu} \mathbf{Q}_{y_s} \mathbb{I}_{\phi_{x_s}} + \mathbb{I}_{\phi_{y_s}}^{\mathrm{T}} \mathbf{Q}_{x_s}^{\mathrm{T}} \mathbb{V}_s^{\mu} \mathbf{Q}_{x_s} \mathbb{I}_{\phi_{y_s}} \right) \\
& + k^2 \Bigg[ \frac{1}{r_1} \left( \frac{1}{r_1} \mathbb{I}_{u_s}^{\mathrm{T}} \mathbb{V}_s^{\mu} \mathbb{I}_{u_s} - \mathbb{I}_{u_s}^{\mathrm{T}} \mathbb{V}_s^{\mu} \mathbf{Q}_{x_s} \mathbb{I}_{w_s} - \mathbb{I}_{u_s}^{\mathrm{T}} \mathbb{V}_s^{\mu} \mathbb{I}_{\phi_{x_s}} - \mathbb{I}_{w_s}^{\mathrm{T}} \mathbf{Q}_{x_s}^{\mathrm{T}} \mathbb{V}_s^{\mu} \mathbb{I}_{u_s} - \mathbb{I}_{\phi_{x_s}}^{\mathrm{T}} \mathbb{V}_s^{\mu} \mathbb{I}_{u_s} \right) \\
& + \mathbb{I}_{w_s}^{\mathrm{T}} \mathbf{Q}_{x_s}^{\mathrm{T}} \mathbb{V}_s^{\mu} \mathbf{Q}_{x_s} \mathbb{I}_{w_s} + \mathbb{I}_{w_s}^{\mathrm{T}} \mathbf{Q}_{x_s}^{\mathrm{T}} \mathbb{V}_s^{\mu} \mathbb{I}_{\phi_{x_s}} + \mathbb{I}_{\phi_{x_s}}^{\mathrm{T}} \mathbb{V}_s^{\mu} \mathbf{Q}_{x_s} \mathbb{I}_{w_s} + \mathbb{I}_{\phi_{x_s}}^{\mathrm{T}} \mathbb{V}_s^{\mu} \mathbb{I}_{\phi_{x_s}} \\
& + \frac{1}{r_2} \left( \frac{1}{r_2} \mathbb{I}_{v_s}^{\mathrm{T}} \mathbb{V}_s^{\mu} \mathbb{I}_{v_s} - \mathbb{I}_{v_s}^{\mathrm{T}} \mathbb{V}_s^{\mu} \mathbf{Q}_{y_s} \mathbb{I}_{w_s} - \mathbb{I}_{v_s}^{\mathrm{T}} \mathbb{V}_s^{\mu} \mathbb{I}_{\phi_{y_s}} - \mathbb{I}_{w_s}^{\mathrm{T}} \mathbf{Q}_{y_s}^{\mathrm{T}} \mathbb{V}_s^{\mu} \mathbb{I}_{v_s} - \mathbb{I}_{\phi_{y_s}}^{\mathrm{T}} \mathbb{V}_s^{\mu} \mathbb{I}_{v_s} \right) \\
& + \mathbb{I}_{w_s}^{\mathrm{T}} \mathbf{Q}_{y_s}^{\mathrm{T}} \mathbb{V}_s^{\mu} \mathbf{Q}_{y_s} \mathbb{I}_{w_s} + \mathbb{I}_{w_s}^{\mathrm{T}} \mathbf{Q}_{y_s}^{\mathrm{T}} \mathbb{V}_s^{\mu} \mathbb{I}_{\phi_{y_s}} + \mathbb{I}_{\phi_{y_s}}^{\mathrm{T}} \mathbb{V}_s^{\mu} \mathbf{Q}_{y_s} \mathbb{I}_{w_s} + \mathbb{I}_{\phi_{y_s}}^{\mathrm{T}} \mathbb{V}_s^{\mu} \mathbb{I}_{\phi_{y_s}} \Bigg] \Bigg\}
\end{aligned} \tag{C.6}$$

## Appendix D. Structural coupling of the host panel and the piezo-patches

To structurally couple the base panel and the piezo-patches, compatibility equations need to be written at the connection boundaries. For that purpose, it is possible to refine the sampling points of the host panel such that the refined sampling points will coincide the sampling points of the piezo-patches as shown in Fig. D.8.

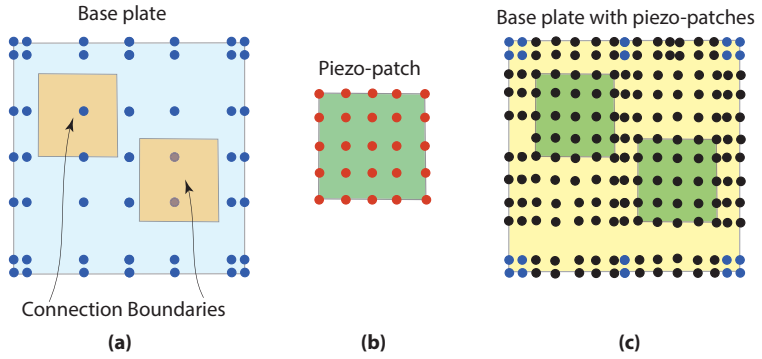


Figure D.8: Sampling point refinement for structural coupling of the host panel and the piezo-patches: **(a)** Gauss-Lobatto sampling of the host panel, **(b)** Gauss-Lobatto sampling of the piezo-patches, and **(c)** refined sampling points of the host panel. Blue dots represent the original sampling points of the base panel, red dots show the sampling points of the piezo-patches, and black dots are the refined sampling points of the base panel.

Using the (extended) forward and backward transformation matrices, a relation between the original and refined sampling points of the base panel can be written as:

$$\mathbf{q}_s^* = \mathbf{\Gamma}_{B_s}^* \mathbf{a}_s = \mathbf{\Gamma}_{B_s}^* \mathbf{\Gamma}_{F_s} \mathbf{q}_s \tag{D.1}$$

Here, $\mathbf{\Gamma}_{B_s}^*$ is the $(N_x N_y)_s \times (N_x N_y)_s$ refined extended transformation matrix.

## References


[1] V. Birman, L. W. Byrd, Modeling and analysis of functionally graded materials and structures, Applied Mechanics Reviews 60 (5) (2007) 195–216.
[2] H.-S. Shen, Functionally Graded Materials: Nonlinear Analysis of Plates and Shells, CRC Press, 2009.
[3] K. Swaminathan, D. T. Naveenkumar, A. M. Zenkour, E. Carrera, Stress, vibration and buckling analyses of FGM plates-A state-of-the-art review, Composite Structures 120 (2015) 10–31.
[4] A. Reichardt, A. A. Shapiro, R. Otis, R. P. Dillon, J. P. Borgonia, B. W. McEnerney, P. Hosemann, A. M. Beese, Advances in additive manufacturing of metal-based functionally graded materials, International Materials Reviews (2020) 1–29.
[5] A. J. Goupee, S. S. Vel, Optimization of natural frequencies of bidirectional functionally graded beams, Structural and Multidisciplinary Optimization 32 (6) (2006) 473–484.
[6] F. Tornabene, A. Liverani, G. Caligiana, FGM and laminated doubly curved shells and panels of revolution with a free-form meridian: A 2-D GDQ solution for free vibrations, International Journal of Mechanical Sciences 53 (6) (2011) 446–470.
[7] J. Huang, G. M. Fadel, V. Y. Blouin, M. Grujicic, Bi-objective optimization design of functionally gradient materials, Materials & Design 23 (7) (2002) 657–666.
[8] L. F. Qian, R. C. Batra, Design of bidirectional functionally graded plate for optimal natural frequencies, Journal of Sound and Vibration 280 (1-2) (2005) 415–424.
[9] B. Sobhani Aragh, H. Hedayati, E. Borzabadi Farahani, M. Hedayati, B. S. Aragh, H. Hedayati, E. B. Farahani, M. Hedayati, B. Sobhani Aragh, H. Hedayati, E. Borzabadi Farahani, M. Hedayati, A novel 2-D six-parameter power-law distribution for free vibration and vibrational displacements of two-dimensional functionally graded fiber-reinforced curved panels, European Journal of Mechanics - A/Solids 30 (6) (2011) 865–883.
[10] K. Maalawi, Optimization of Functionally Graded Material Structures: Some Case Studies, in: Optimum Composite Structures, IntechOpen, 2019.
[11] Y. Kiani, M. Sadighi, M. R. Eslami, Dynamic analysis and active control of smart doubly curved FGM panels, Composite Structures 102 (2013) 205–216.

[12] B. A. Selim, L. W. Zhang, K. M. Liew, Active vibration control of FGM plates with piezoelectric layers based on Reddy's higher-order shear deformation theory, Composite Structures 155 (2016) 118–134.
[13] J. S. Moita, A. L. Araújo, V. F. Correia, C. M. Mota Soares, J. Herskovits, Material distribution and sizing optimization of functionally graded plate-shell structures, Composites Part B: Engineering 142 (2018) 263–272.
[14] F. Tornabene, N. Fantuzzi, M. Bacciocchi, The local GDQ method applied to general higher-order theories of doubly-curved laminated composite shells and panels: The free vibration analysis, Composite Structures 116 (1) (2014) 637–660.
[15] A. M. A. Neves, A. J. M. Ferreira, E. Carrera, M. Cinefra, C. M. C. Roque, R. M. N. Jorge, C. M. M. Soares, Static, free vibration and buckling analysis of isotropic and sandwich functionally graded plates using a quasi-3D higher-order shear deformation theory and a meshless technique, Composites Part B: Engineering 44 (1) (2013) 657–674.
[16] T. Mori, K. Tanaka, Average stress in matrix and average elastic energy of materials with misfitting inclusions, Acta Metallurgica 21 (5) (1973) 571–574.
[17] S. S. Vel, R. C. Batra, Three-dimensional exact solution for the vibration of functionally graded rectangular plates, Journal of Sound and Vibration 272 (3-5) (2004) 703–730.
[18] K. Mercan, A. K. Baltacioglu, Ö. Civalek, A. Kemal, Free vibration of laminated and FGM/CNT composites annular thick plates with shear deformation by discrete singular convolution method, Composite Structures 186 (November 2017) (2018) 139–153.
[19] T. Bailey, J. E. Hubbard, Distributed piezoelectric-polymer active vibration control of a cantilever beam, Journal of Guidance, Control, and Dynamics 8 (5) (1985) 605–611.
[20] D. Casagrande, P. Gardonio, M. Zilletti, Smart panel with time-varying shunted piezoelectric patch absorbers for broadband vibration control, Journal of Sound and Vibration 400 (2017) 288–304.
[21] U. Aridogan, I. Basdogan, A. Erturk, Multiple patch-based broadband piezoelectric energy harvesting on plate-based structures, Journal of Intelligent Material Systems and Structures 25 (14) (2014) 1664–1680.
[22] M. M. Gozum, A. Aghakhani, G. Serhat, I. Basdogan, Electroelastic modeling of thin-laminated composite plates with surface-bonded piezo-patches using Rayleigh - Ritz method, Journal of Intelligent Material Systems and Structures 29 (10) (2018) 2192–2205.
[23] X. Han, M. Neubauer, J. J. Wallaschek, Improved piezoelectric switch shunt damping technique using negative capacitance, Journal of Sound and Vibration 332 (1) (2013) 7–16.
[24] P. L. Motlagh, A. Aghakhani, I. Basdogan, Passive vibration control of a plate via piezoelectric shunt damping with fem and ecm, in: Smart Materials and Nondestructive Evaluation for Energy Systems IV, Vol. 10601, International Society for Optics and Photonics, 2018, p. 1060103.
[25] C. K. Lee, Theory of laminated piezoelectric plates for the design of distributed sensors/actuators. Part I: Governing equations and reciprocal relationships, Journal of the Acoustical Society of America 87 (3) (1990) 1144–1158.
[26] X. Q. He, K. M. Liew, T. Y. Ng, S. Sivashanker, A FEM model for the active control of curved FGM shells using piezoelectric sensor/actuator layers, International Journal for Numerical Methods in Engineering 54 (6) (2002) 853–870.
[27] C. De Marqui Junior, A. Erturk, D. J. Inman, An electromechanical finite element model for piezoelectric energy harvester plates, Journal of Sound and Vibration 327 (1-2) (2009) 9–25.
[28] H. F. Tiersten, Linear Piezoelectric Plate Vibrations: Elements of the Linear Theory of Piezoelectricity and the Vibrations Piezoelectric Plates, Springer, 2013.
[29] U. Aridogan, I. Basdogan, A. Erturk, Random vibration energy harvesting on thin plates using multiple piezopatches, Journal of Intelligent Material Systems and Structures 27 (20) (2016) 2744–2756.
[30] A. Aghakhani, P. Lahe Motlagh, B. Bediz, I. Basdogan, A general electromechanical model for plates with integrated piezo-patches using spectral-Tchebychev method, Journal of Sound and Vibration 458 (2019) 74–88.
[31] P. L. Motlagh, B. Bediz, I. Basdogan, A spectral Tchebychev solution for electromechanical analysis of thin curved panels with multiple integrated piezo-patches, Journal of Sound and Vibration 486 (2020) 115612.
[32] A. Darabi, M. Leamy, Piezoelectric T-matrix development and multiple scattering analysis of electroacoustic wave propagation in thin plates, Proceedings of the ASME Design Engineering Technical Conference 8.
[33] A. Darabi, M. J. Leamy, Analysis and experimental verification of multiple scattering of acoustoelastic waves in thin plates for enhanced energy harvesting, Smart Materials and Structures 26 (8) (2017) 085015.
[34] H. Yoon, B. D. Youn, H. S. Kim, Kirchhoff plate theory-based electromechanically-coupled analytical model considering inertia and stiffness effects of a surface-bonded piezoelectric patch, Smart Materials and Structures 25 (2).
[35] E. Carrera, S. Brischetto, M. Cinefra, S. Brischetto, Variable kinematics and advanced variational statements for free vibrations analysis of piezoelectric plates and shells, CMES - Computer Modeling in Engineering and Sciences 65 (3) (2010) 259–341.
[36] M. D'Ottavio, D. Ballhause, B. Kröplin, E. Carrera, Closed-form solutions for the free-vibration problem of multilayered piezoelectric shells, Computers and Structures 84 (22-23) (2006) 1506–1518.
[37] K. M. Liew, X. Q. He, T. Y. Ng, S. Kitipornchai, Active control of FGM shells subjected to a temperature gradient via piezoelectric sensor/actuator patches, International Journal for Numerical Methods in Engineering 55 (6) (2002) 653–668.
[38] R. Mirzaeifar, H. Bahai, S. Shahab, Active control of natural frequencies of FGM plates by piezoelectric sensor/actuator pairs, Smart Materials and Structures 17 (4).
[39] M. Shariyat, Dynamic buckling of suddenly loaded imperfect hybrid FGM cylindrical shells with temperature-dependent material properties under thermo-electro-mechanical loads, International Journal of Mechanical Sciences 50 (12) (2008) 1561–1571.
[40] M. Shariyat, Vibration and dynamic buckling control of imperfect hybrid FGM plates with temperature-dependent material properties subjected to thermo-electro-mechanical loading conditions, Composite Structures 88 (2) (2009) 240–252.
[41] E. Carrera, S. Valvano, Analysis of laminated composite structures with embedded piezoelectric sheets by variable kine-

matic shell elements, Journal of Intelligent Material Systems and Structures 28 (20) (2017) 2959–2987.
[42] E. Carrera, S. Valvano, G. M. Kulikov, Electro-mechanical analysis of composite and sandwich multilayered structures by shell elements with node-dependent kinematics, International Journal of Smart and Nano Materials 9 (1) (2018) 1–33.
[43] S.-H. Chi, Y.-L. Chung, Mechanical behavior of functionally graded material plates under transverse load - Part I: Analysis, International Journal of Solids and Structures 43 (13) (2006) 3657–3674.
[44] M. R. Anamagh, B. Bediz, Free vibration and buckling behavior of functionally graded porous plates reinforced by graphene platelets using spectral Chebyshev approach, Composite Structures 253 (July) (2020) 112765.
[45] F. Tornabene, Free vibration analysis of functionally graded conical, cylindrical shell and annular plate structures with a four-parameter power-law distribution, Computer Methods in Applied Mechanics and Engineering 198 (37-40) (2009) 2911–2935.
[46] D. Gottlieb, S. A. Orszag, Numerical Analysis of Spectral Methods, Theory and Applications, SIAM-CBMS, Philedelphia, PA, 1977.
[47] B. Yagci, S. Filiz, L. L. A. Romero, O. B. Ozdoganlar, A spectral-Tchebychev technique for solving linear and nonlinear beam equations, Journal of Sound and Vibration 321 (1-2) (2009) 375–404.
[48] B. Bediz, A spectral-Tchebychev solution technique for determining vibrational behavior of thick plates having arbitrary geometry, Journal of Sound and Vibration 432 (2018) 272–289.
[49] G. Serhat, B. Bediz, I. Basdogan, Unifying lamination parameters with spectral-Tchebychev method for variable-stiffness composite plate design, Composite Structures 242 (June 2019) (2020) 112183.